Purely Elastic Fluid–Structure Interactions in Microfluidics: Implications for Mucociliary Flows

Cameron C. Hopkins, Simon J. Haward, and Amy Q. Shen*

Fluid–structure interactions lie at the heart of the complex, and often highly coordinated, motions of actively driven microscale biological systems (e.g., translating cilia, flagella, and motile cells). Due to the highly viscoelastic nature of most relevant biological fluids and the small length scales involved, the viscous and inertial forces in such flows are dominated by elasticity. However, elastic effects are often overlooked in studies seeking to address phenomena like the synchronization of beating cilia. In this study, unique microfluidic experiments are presented to demonstrate that inertia-free viscoelastic flows can lead to highly regular beating of an immersed (passive) flexible structure, herein named "purely-elastic" fluid–structure interaction. It is also shown how two such flexible structures can achieve an extraordinary degree of synchronization, with a correlation coefficient approaching unity. The synchronization is a result of the generation of localized elastic stresses in the fluid that effectively link the two objects. These purely elastic interactions may be important to consider toward developing a complete understanding of the motions of microscale biological systems.

1. Introduction

Microfluidics has emerged as a powerful tool in biomedical research and for modeling various aspects of biological systems, revealing new insights into complex problems.[1–3] One unexplored territory to which microfluidics has the potential to contribute is the understanding of synchronized or coupled motions of translating motile objects, cells, bacteria, cilia, etc., in biological fluids. Flows of simple, Newtonian fluids (like water) around objects are described by the ratio of the inertial to viscous forces through the Reynolds number $Re = \rho V R / \eta$, where ρ and η are the fluid density and viscosity, respectively, V is a typical flow velocity and R is a typical lengthscale, such as the radius of the object. However, most biological fluids (e.g., mucus, semen, synovial fluid) are viscoelastic in nature, meaning they possess properties intermediate between viscous liquids and elastic solids. The fluid elasticity arises

from the deformation and relaxation of suspended polysaccharides, mucins, or other macromolecules, and the elastic response of the fluid depends strongly upon the timescale (or lengthscale) of the deforming flow field. The Weissenberg number ($Wi = \lambda V / R$) describes the ratio of elastic to viscous forces in flow, where λ is the relaxation time of the fluid and V/R represents a typical deformation rate (or an inverse timescale) associated with the flow field. At the small lengthscale of (e.g., a cilium) $R = O$ (1 µm), Reynolds numbers are consequently small, indicating that inertia is negligible.[4,5] However, the Weissenberg number can be simultaneously high, leading to strong elastic forces that can yield extremely complex and counterintuitive nonlinear flow phenomena like elastic instabilities and elastic turbulence in the absence of inertia.[6–8] A useful dimensionless quantity for considering such flows is the elasticity number, $El = Wi/Re = \lambda \eta / \rho R^2$, which can be interpreted as either the ratio of relaxation time to diffusion time, or as the ratio of elastic to inertial forces in the flow. Although mucus properties can vary widely depending on many factors, taking representative values quoted for the relaxation time ($0.01 < \lambda < 1$ s), viscosity ($0.01 < \eta < 1$ Pa s) and density ($\rho \approx 1000$ kg m^{-3}), an estimate for the elasticity number for flow around a cilium is $10^5 < El < 10^9$.[9,10] Such a high figure suggests that elastic forces completely dominate the flow.

The study of fluid–structure interactions (FSI) in nonlinear Newtonian flows is a well-established field. Well-known phenomena arise due to the onset of flow unsteadiness at high Re, such as the vortex-induced vibrations that must be accounted for in the design of large engineering structures like bridges, oil-rig platforms, and tall towers. However, the understanding of how nonlinearities due to fluid elasticity in high Wi viscoelastic flows are manifested in the deformation of flexible structures (viscoelastic FSI) is a topic in its infancy.[11,12] Such interactions are likely to be key to understanding the motions of cells, cilia, and other microscopic objects in biological media. Nonetheless, for fairly obvious reasons of experimental difficulty, most studies of cilia motion and interactions have been performed theoretically or by numerical simulation, and these largely ignore the viscoelastic properties of mucus, focusing instead on low Re hydrodynamic effects.[13–15] The work of Dey et al., conducted in macroscale apparatus containing stretched elastic sheets[11] and flexible polymeric cylinders,[12] was the first to report on feedback between viscoelastic flow instabilities and deformation of immersed structures. For flow past a deformable cylinder (pinned by both ends to the channel walls)

Dr. C. C. Hopkins, Dr. S. J. Haward, Prof. A. Q. Shen
Okinawa Institute of Science and Technology Graduate University
Onna-son, Okinawa 904-0495, Japan
E-mail: amy.shen@oist.jp

The ORCID identification number(s) for the author(s) of this article can be found under https://doi.org/10.1002/smll.201903872.

**ADVANCED
SCIENCE NEWS**
www.advancedsciencenews.com

NANO · MICRO
small
www.small-journal.com

the authors reported regimes of steady displacement, followed by 1D, then 2D motions of the cylinder midsection as they increased Wi.[12] The 1D and 2D oscillatory motion was associated with accumulation and release of elastic stresses in the downstream wake of the cylinder (with no clear characteristic frequency), while the 2D behavior was accompanied by a strong asymmetry in the flow around the sides of the cylinder, which pulled the structure away from the flow axis.[12]

In this work, we fabricate free-standing microfluidic circular cylinders using a state-of-the-art glass etching technique (selective laser-induced etching, SLE)[16,17] and we present the first example of viscoelastic FSI in a microfluidic geometry. The passive (i.e., nondriven) cantilevered posts represent scale models of cilia. Although they have larger radii ($R \approx 20$ μm) than real cilia, we select a model viscoelastic fluid with the necessary high viscosity and relaxation time to obtain a high elasticity number ($El \approx 10^8$) comparable with that expected in a real mucociliary flow. In earlier work,[18] we have characterized in detail the flow of the model fluid around similar, but rigidly pinned, microposts in order to understand the nature of the flow instabilities that occur with increasing Wi. Here we examine how those instabilities interact not only with a single cantilevered post, but also with two posts aligned in the flow direction. High speed imaging is used to track the motion of the posts, and quantitative high speed flow velocimetry and birefringence imaging are used to understand how the flow field, stress field, and post motion all interact over a wider range of Weissenberg numbers ($0.01 < Wi < 2000$) than has been possible previously. Various regimes of interaction are found between the flowing fluid and the posts. In particular, at intermediate Wi the motion of the single post becomes time-dependent, and in contrast to previous work in this area, exhibits a clear periodicity equal to the fluid relaxation time. In addition, at similar Wi, we show for the first time how the time-dependent motion of two aligned posts can become strongly correlated in an unsteady viscoelastic flow. These effects are explained by the presence of a localized strand of high elastic stress that originates from the trailing wake of the upstream post and effectively links the two posts together.

2. Results and Discussion

2.1. Microfluidic Devices

Schematic diagrams of the two microfluidic channels used in this work (not to scale), are shown in **Figure 1**a,b, also indicating the coordinate systems employed in each device. Details of their fabrication are discussed in the Experimental Section. Figure 1c–f shows micrographs of the fused silica channels along with the measured dimensions. Both channels have height $H = 2000$ μm and width $W = 400$ μm. One of the channels, called "SC," has a single cantilevered cylinder (diameter $2R = 32.0$ μm, length $L = 1940$ μm) situated in the channel center. The second, called "DC," has two cantilevered cylinders (both $2R = 34.5$ μm, length $L = 1960$ μm) aligned on the channel centerline and spaced 400 μm apart. In the DC channel, the upstream cylinder will be referred to as DC_1 and the downstream cylinder as DC_2.
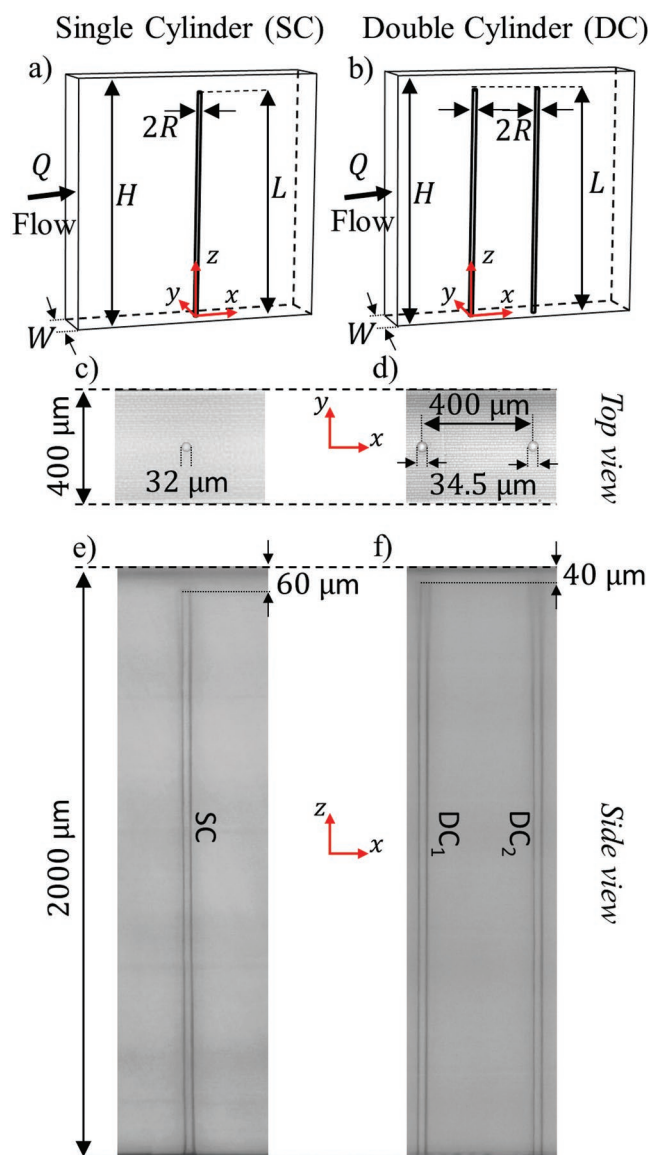
Figure 1. Experimental flow geometries: a,b) Schematic diagrams (not to scale) of the single cylinder (SC) and double cylinder (DC) channels, respectively. In the DC channel, the upstream and downstream cylinders are referred to as DC_1 and DC_2, respectively. The coordinate systems are indicated with the origin located at the base of the most upstream post. c,d) Micrographs taken focused on the detached end of the posts in the SC and DC channels, respectively. The measured diameters of the posts, and the center to center distance between DC_1 and DC_2, are indicated. e,f) Side view micrographs of the posts indicating the measured channel height and the gap between the channel wall and the free ends of the posts.

2.2. Linear Deflection in Newtonian Control Experiments

We begin by conducting control experiments investigating the linear deflection of the microcylinders arising from the flow of a Newtonian liquid. Owing to the length scale of the system and viscosity of the Newtonian liquid used, all of the experiments shown here have negligible $Re \ll 1$.

Since the aspect ratio of the cylinders is large, i.e., $L/R \gg 1$, the cylinders can be considered slender rods. For low-Reynolds

ADVANCED
SCIENCE NEWS
www.advancedsciencenews.com

NANO · MICRO
small
www.small-journal.com

number flows, the drag force experienced by a slender rod in a viscous liquid flowing at speed V is given by[19]

$$F_D = \frac{8\pi\eta LV}{\ln\left(\frac{L}{R}\right)} \tag{1}$$

Equation (1) assumes uniform force per unit length on the cylinder, which is a reasonable assumption given the high channel aspect ratio of our devices, $\alpha = H/W = 5$. The drag force will deflect the cylinder in the flow direction until the elastic restoring force of the cylinder balances the viscous drag. Using Euler–Bernoulli beam theory, the linear deflection Δx of the free end of the cantilevered cylinder is given by[20]

$$\Delta x = \frac{L^3}{8EI} F_D \tag{2}$$

where $E = 73$ GPa is the Young's modulus of fused silica,[21] and $I = \pi R^4/4$ is the 2nd moment of area of a circular cylinder. Equation (2) can be rearranged into the Hookean force equation

$$F_D = k\Delta x \tag{3}$$

where $k = 8EI/L^3$. For the cylinder in the SC channel, the bending stiffness $EI = 3.76$ nN m^2 and $k = 4.1$ N m^{-1}. The natural frequency of the cylinder can be approximated from $f_n = \sqrt{k/m}$, where m is the mass of the cylinder, yielding $f_n = 34.5$ kHz. We note that this defines a timescale for the dynamics of the cylinder that is much faster than the fluid relaxation time ($\lambda = 1.3$ s). Therefore, we can expect that the time-dependent behavior in our system should be completely dominated by fluid elasticity. Combining Equations (1) and (2), the linear deflection of the tip of a cantilevered fused silica microcylinder subject to low-Reynolds number viscous flow is approximated by

$$\Delta x = \frac{1.8\pi\eta L^4}{HWEI \ln(L/R)} Q \tag{4}$$

Here we take $V = 1.8 Q/WH$, where Q is the volumetric flow rate and the factor 1.8 accounts for the maximum of the parabolic velocity profile in a channel of $\alpha = 5$ (since the cylinder is located on the channel centerline).

The measured streamwise strain (X/L) of the posts from their initial resting positions due to the flow of a Newtonian 95 wt% Glycerol–Water solution is shown in **Figure 2**. The top-left inset of Figure 2a shows a composite image formed from two video frames, showing the change in position of the tip of the SC cylinder from left to right when the flow rate is increased from $Q_1 = 0$ mL min^{-1} to $Q_2 = 0.9$ mL min^{-1}. The center of the cylinder tip is tracked through the whole video by thresholding and finding the center-of-mass of the bright pixels belonging to the cylinder (see the Experimental Section). The bottom right inset of Figure 2a shows the resulting measured displacement of the tip of the SC cylinder as Q is incremented from 0 up to 1.0 mL min^{-1} in steps of 0.1 mL min^{-1}, with each flow rate being held constant for 10 s. After each step change in Q, ≈3 s is required
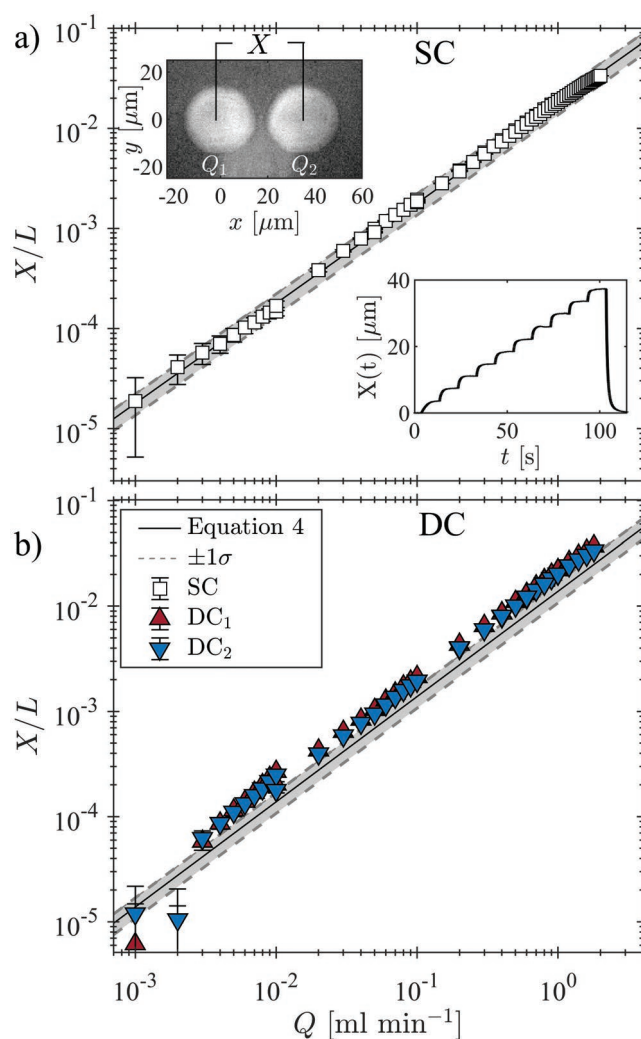
Figure 2. Low Re Newtonian control experiments using 95 wt% glycerol solution. a) SC post strain as a function of the imposed volumetric flow rate and compared with the prediction of Equation (4). Top-left insert shows a composite snapshot illustrating the displacement of the post when the flow rate is increased from $Q_1 = 0$ mL min^{-1} to $Q_2 = 0.9$ mL min^{-1}. Bottom-right insert shows stepwise increments in post displacement for 10 stepwise increases in flowrate from $Q = 0$ mL min^{-1} to $Q = 1$ mL min^{-1}. b) Deflection of the free ends of DC$_1$ and DC$_2$ as a function of the imposed volumetric flow rate and compared with the prediction of Equation (4).

for the deflection of the cylinder to equilibrate at the new flow rate and the post-transient steady state position is recorded. The strain of the cylinders in both the SC and DC channels is plotted in Figure 2a,b, respectively, for flow rates $10^{-3} \leq Q \leq 2.0$ mL min^{-1} ($Re < 0.02$). The linear strain of the cylinders predicted by Equation (4) is plotted as the black line, where the shaded gray region represents a ±1 standard deviation uncertainty due to estimated measurement errors in the precise device dimensions and fluid viscosity. For the SC channel, the measured strain agrees with Equation (4) extremely well. For the DC channel, over most of the flow rate range, the magnitude of the measured strains is within ≈1 standard deviation of the model prediction and displays the expected linear trend.

ADVANCED
SCIENCE NEWS
www.advancedsciencenews.com

NANO · MICRO
small
www.small-journal.com
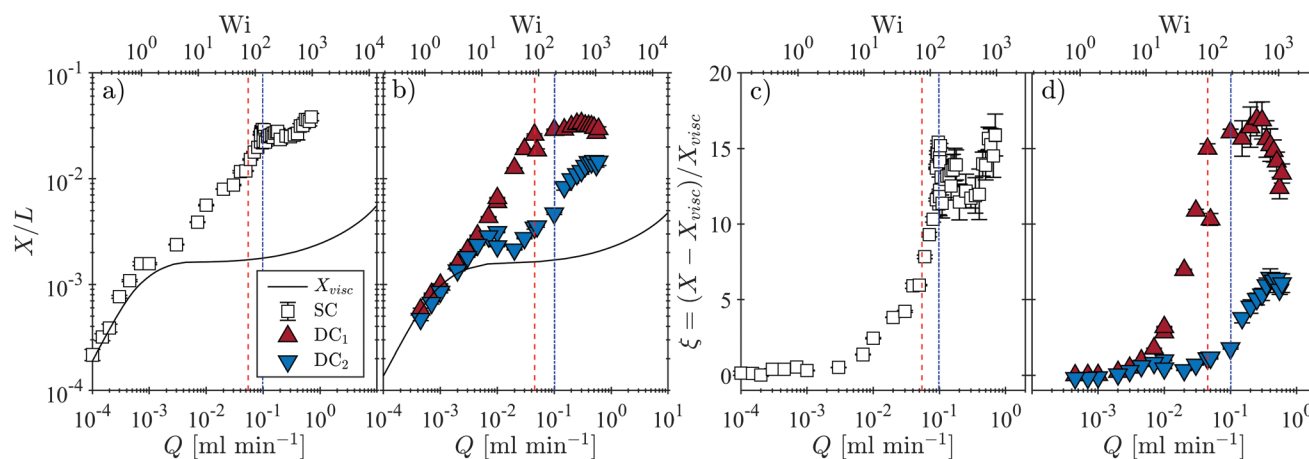
Figure 3. Streamwise strain of the flexible posts in a shear-banding viscoelastic WLM solution. (a) and (b) measured streamwise strain of the posts in the SC and DC channels, respectively, over a range of imposed flow rate or Weissenberg number. The solid black lines indicate a numerical prediction of the strain due to the shear-thinning viscosity of the fluid using an inelastic GNF model. (c) and (d) show the relative contribution of elasticity to the stress on the cylinders (Equation (5)) in the SC and DC channels, respectively. The vertical dashed red and dashed–dotted blue lines mark the onset of asymmetric and time-dependent flows in the WLM solution, respectively.

2.3. Nonlinear Deflection and Fluid–Structure Interactions in Viscoelastic Flow

2.3.1. Deflection of the Flexible Cylinders

Having confirmed that the cantilevered posts in both the SC and DC flow channels respond predictably in low Re Newtonian flow, we now proceed to examine their response to a more complex shear-banding viscoelastic wormlike micellar (WLM) fluid (also at very low $Re < 10^{-5}$). WLM solutions are composed of self-assembled surfactant aggregates and have been considered as models of complex biological fluids containing associating lipids, proteins, or peptides.[22] The same WLM solution as used here has been previously studied in flow around similar slender (but rigid) microposts fixed to both the top and bottom channel walls.[18] In that study, the flow of the WLM fluid upstream of the cylinder was found to be uniform and plug-like along nearly the full width and depth of the channel. In addition, for imposed Wi less than a critical value $Wi_1 \approx 60$, the flow remained steady and was laterally symmetric about $y = 0$. Above Wi_1, the flow destabilized and became laterally asymmetric (though remained steady), with the bulk of the fluid flowing preferentially around one side of the post. The handedness of the asymmetry was random, and the instability was described as a supercritical pitchfork bifurcation, likely resulting from a combination of the strong shear thinning and the elasticity of the fluid.[18] Above a second higher critical Weissenberg number $Wi_2 \approx 130$ the asymmetric flow became time dependent with a characteristic time close to the Maxwellian relaxation time (λ), due to Hopf bifurcation. In the current experiments using similar, but flexible, microposts, analogous transitions are observed. Interestingly, however, the critical Weissenberg numbers for the transitions are found to be slightly higher in the flexible post geometries, with an apparent stabilization of the flow in the compliant systems. In the SC system $Wi_1 \approx 75$ and $Wi_2 \approx 145$. For the DC system $Wi_1 \approx 85$ and $Wi_2 \approx 190$. We note that Dey et al[12] did not report a regime of steady asymmetry in

their flexible post experiments, which transitioned from steady to 1D (laterally symmetric) oscillations, before a final transition to a time-dependent asymmetric state. However, they also reported that instabilities arose at a higher critical Weissenberg numbers for flexible compared with rigid posts. Our results indicate that there may be an additive effect as the number of flexible posts is increased.

In **Figure 3**a,b, we present the measured strain of the SC post and the two DC posts, respectively. In the plots, Wi_1 and Wi_2 are indicated by the dashed red and dashed–dotted blue lines, respectively. For the SC and DC_1 posts, there is an almost linear, Newtonian-like increase of the post strain along the streamwise direction as the flow rate is increased from a low value. Beyond the onset of asymmetric flow, the posts become deflected off axis and the streamwise strain tends to saturate. The DC_2 post responds differently, initially increasing its strain equivalently to DC_1 up to an intermediate Wi, before leveling to a short plateau. The streamwise strain of DC_2 increases again at higher Wi, subsequent to the onset of asymmetric flow.

Since the WLM solution is a shear thinning viscoelastic fluid (see rheological characterization in the Supporting Information), Equation (4) cannot be used to accurately predict the resulting deflection of a cylinder at a given flow rate. In order to separate viscous from elastic effects in our experimental data, we fitted the Carreau–Yasuda generalized Newtonian fluid (GNF) model to the steady shear rheology of the WLM solution (see Supporting Information) and used the model in 2D numerical simulations of the flow past a cylinder using COMSOL Multiphysics (see the Experimental Section). The GNF model employed describes the shear thinning viscosity of the fluid but does not account for elasticity, so enables calculation of only the viscous stress on the cylinders as a function of flow rate. Note also that in this simple inelastic model the flow remains always steady and symmetric. The resulting numerically predicted deflection is denoted X_{visc} and is plotted in Figure 3a,b as solid black curves. At low flow rate, X_{visc} has a constant positive slope (pseudo-Newtonian behavior) and predicts the measured

**ADVANCED
SCIENCE NEWS**
www.advancedsciencenews.com

**NANO · MICRO
small**
www.small-journal.com

tip deflection well. At intermediate flow rates, corresponding to $Wi \gtrsim 1$, the strong shear thinning of the fluid becomes manifested and X_{visc} reaches a plateau value. Here, elastic stress, not accounted for by the model, begins to dominate and the measured tip displacement deviates strongly from the model prediction. Interestingly, for the SC and DC_1 posts in particular, the deflection continues to increase in a pseudo-Newtonian manner. This suggests that the magnitude of the elastic stress generated with increasing flow rate is approximately equivalent to the amount of viscous stress absent due to shear thinning.

We quantify the elastic contribution to the stress on the cylinder by defining an effective elasticity parameter

$$\xi = \frac{X - X_{visc}}{X_{visc}} \tag{5}$$

which is plotted for the SC and DC cylinders in Figure 3c,d, respectively. The plots confirm that at low flow rates the cylinder is largely subjected to viscous force, and $\xi \approx 0$. For the SC and DC_1 posts, the elastic stress increases markedly beyond $Wi \approx 1$ and continues to increase until the onset of asymmetry and time dependence. At flow rates beyond the onset of asymmetry at Wi_1, the post moves off axis and the comparison with the GNF model prediction breaks down. Beyond the onset of time dependence, ξ attains large error bars due to unsteady motions of the post which will be described in detail subsequently. For DC_2, the elastic stress remains low until $Wi \approx Wi_1$, before increasing steadily and appearing to saturate to a plateau value in the time-dependent region.

2.3.2. Flow Visualization and Flow-Induced Birefringence

Time-averaged flow velocimetry (μ-PIV) and flow-induced birefringence (FIB) results at three Wi characteristic of the different flow regimes (i.e., steady symmetric, steady asymmetric, and time-dependent) are shown in **Figure 4**, where the white circles indicate the resting positions of the cylinders. For $Wi < 1$, the flow field measured by μ-PIV is both fore-aft and laterally symmetric, and no FIB can be measured. For $1 < Wi < Wi_1$ (example shown in Figure 4a,b), the flow remains steady and laterally symmetric about $y = 0$, but a long wake of low flow velocity forms downstream of the cylinder that grows in length with increasing Wi. The long wake is also visible as an intense region of FIB that indicates strong micellar alignment and high tensile elastic stress in the fluid. The images in Figure 4a,b illustrate the flow at a Wi just below Wi_1. Under these conditions, the wake of DC_1 fully coincides with, and envelops, DC_2. As indicated by the FIB, the elastic stress in the wake of DC2 is significantly lower than in the wake of DC_1. Even at this negligible Re, the wake of DC_1 effectively shields or screens DC_2 from the flow field, providing an explanation for the contrasting displacement curves shown in Figure 3b and contrasting elastic response shown in Figure 3d.

The μ-PIV and FIB data shown in Figure 4c,d illustrate the steady asymmetric flow of the WLM fluid around the posts at $Wi_1 < Wi \lesssim Wi_2$. In the case of the SC post, the flow velocity and FIB are comparable with those reported in recent literature for flows of similar viscoelastic fluids around rigid microposts[18]

and around flexible macroscale posts.[12] Qualitatively, the SC and DC results presented here can be described in similar terms; the fluid preferentially flows around one side of each post, while the fluid on the opposite side of the post is effectively stagnant. In both cases, the FIB data reveal a strong degree of micellar alignment and elastic tensile stress on one side of the post and for a significant distance downstream. However, there is an important difference to note: behind the SC post, the region of high FIB signal tends directly toward the sidewall of the channel, but the FIB in the wake of DC_1 is diverted by the flow to coincide with DC_2, only subsequently approaching the channel sidewall further downstream. Note that in Figure 4c–e the μ-PIV images illustrate asymmetric flows with opposite handedness from the corresponding FIB (for presentation purposes the μ-PIV images have been flipped by an inversion of the y-axis). This is simply because the images are not obtained simultaneously, but from separate experiments, and provides an illustration of the random selection of the handedness.

In Figure 4e,f, the flow in both the SC and DC channels is for $Wi \gg Wi_2$ and is both asymmetric and time dependent. However, the images can be described in qualitatively similar terms to those in Figure 4c,d due to time averaging. Movies S1–S6 in which the time-dependence of the measured flow properties is clearly apparent at each $Wi > Wi_1$ are provided in the Supporting Information. In Subsections 2.3.3–2.3.5, we will focus in detail on the dynamics of the time-dependent flows and on the nature of their interactions with the responsive flexible posts.

Time-dependent FIB data imaged through the side of the channel (i.e., through the x-z plane) at three Wi representative of the different unstable flow regimes observed ($Wi_1 < Wi \lesssim Wi_2$, $Wi \gtrsim Wi_2$, and $Wi \gg Wi_2$) are included in the Supporting Information.

2.3.3. Characterization of the Time-Dependent Flow

Here we present a characterization of the time-dependence observed in the μ-PIV and FIB measurements made in the SC channel. The time-dependence of the flow in the DC channel is qualitatively similar and for brevity is not explicitly shown here. To characterize the time dependence in the velocimetry data, we quantify a time-resolved measure of the asymmetry parameter:[18]

$$I = \frac{|u_1 - u_2|}{u_1 + u_2} \tag{6}$$

where u_1 and u_2 are the streamwise component of the velocity at positions $x = 0$, $y = -0.1$ mm and $x = 0$, $y = 0.1$ mm, respectively (i.e., on opposite sides of the post).

Space-time diagrams of the normalized streamwise component of the fluid velocity u along the line $x = 0$ are plotted in **Figure 5**a–d over four representative Weissenberg numbers. The first case shown in Figure 5a is for $Wi \lesssim Wi_1$. Apart from random noise, the flow is steady and symmetric on either side of the cylinder; $u_1 \approx u_2$ and $I \approx 0$ in Figure 5e (black line). For the second case, shown in Figure 5b, $Wi_1 < Wi \lesssim Wi_2$. The flow is steady and asymmetric, with most of the fluid flowing on the negative-y side of the post. Hence, $u_1 \neq u_2$ and the
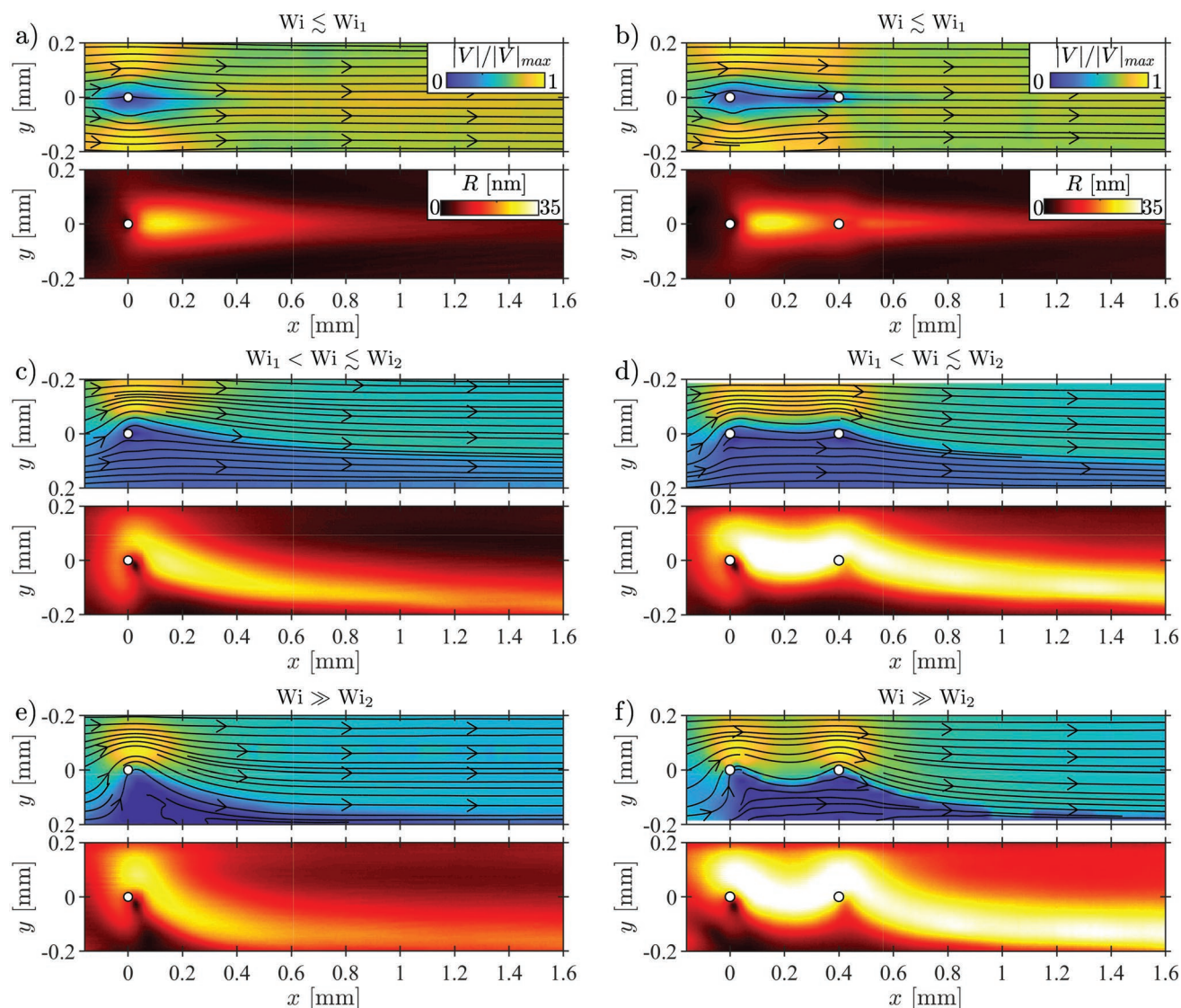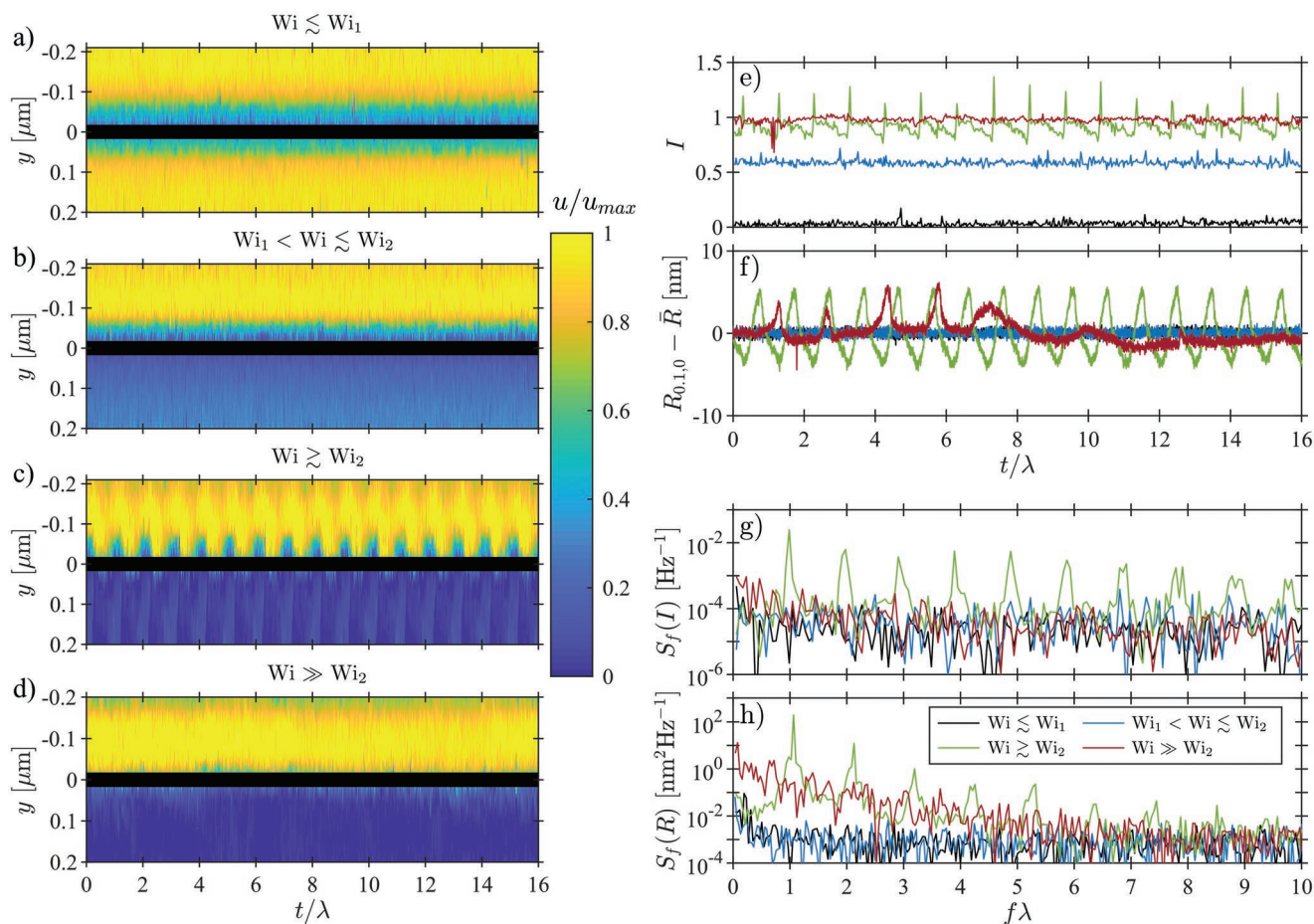
Figure 4. Time averaged results of flow velocimetry (μ-PIV) and corresponding flow-induced birefringence (FIB) in the SC (left) and DC (right) flow channels under different regimes of flow. a,b) Steady symmetric, $Wi \lesssim Wi_1$. c,d) Steady asymmetric, $Wi_1 < Wi \lesssim Wi_2$. e,f) Time dependent, $Wi \gg Wi_2$. Note that although the handedness of the asymmetry is random (see the text), for each PIV-FIB pair the y-axes are plotted to show the same handedness for easy visual comparison. The μ-PIV data are averaged over 20 s and the FIB data are averaged over 40 s. See the Supporting Information for videos of the time-dependent data.

asymmetry parameter shown in Figure 5e for this case (blue line) is between 0 and 1 and is steady in time. In the third case, shown in Figure 5c, $Wi \gtrsim Wi_2$. The flow is now strongly asymmetric, time-dependent, and highly periodic in time. Here, u_2 is much closer to 0 on the positive-y side of the post. In addition, u_2 periodically increases to a small positive value, thus washing away the initially stagnant fluid, before arresting again. When the fluid arrests, it rebounds, and u_2 briefly goes negative. Although not apparent in the spacetime diagram, it is clear in the time series plot of I in Figure 5e (green line) where periodic spikes of $I > 1$ are evident, followed by a gradual decrease. This behavior was also noted in a similar Wi regime for flow around rigid microposts.[18] Finally, in the fourth case shown in Figure 5d, $Wi \gg Wi_2$. The flow is strongly asymmetric but lacks the regular time-dependence as in the previous case. On

the positive-y side of the post $u_2 \approx 0$, with occasional random fluctuations. This results $I \approx 1$ for the entire duration of the experiment (red line in Figure 5e), but the time dependence manifests as random small-scale perturbations on the flow, sometimes resulting in $I > 0$.

We characterize the time dependence of the FIB by analyzing the retardation at the point $x = 0.1$ mm and $y = 0$, denoted $R_{0.1,0}$. This quantity, minus its time-averaged mean $\overline{R}$, is plotted in Figure 5f for the same four representative Wi shown in Figure 5e. For the steady symmetric case at $Wi \lesssim Wi_1$ (black line), a long birefringent wake trails the cylinder that does not vary in time so $R_{0.1,0} - \overline{R} \approx 0$, plus or minus random noise. For the steady asymmetric case at $Wi_1 < Wi \lesssim Wi_2$ (blue line), the asymmetric wake also does not fluctuate in time so again $R_{0.1,0} - \overline{R} \approx 0$. Above the onset of time dependence at

ADVANCED
SCIENCE NEWS
www.advancedsciencenews.com

NANO · MICRO
small
www.small-journal.com

Figure 5. Analysis of time-dependent fluid properties measured in the SC flow channel at four representative values of the Weissenberg number. a–d) Space-time diagrams depicting the streamwise component of the fluid velocity u normalized by its maximum value along the line $x = 0$ for four representative values of the Weissenberg number. The horizontal black bar depicts the approximate rest-position of the cylinder. Time series of the e) flow asymmetry parameter (Equation (6)) and f) the retardation (or FIB) measured at a location 0.1 mm downstream of the cylinder. (g) and (h) show power spectra derived from the time series presented in parts (e) and (f), respectively.

$Wi \gtrsim Wi_2$ (green line) the retardation, and therefore the elastic stress downstream of the cylinder shows an extremely regular periodicity. Note that the curves plotted in Figure 5e,f are from separate nonsimultaneous experiments, therefore the retardation and asymmetry time series are not synchronous. However, the peaks in $I(t)$ occur when the fluid in the stagnant region reverses direction. This backflow, which increases the asymmetry, pulls the birefringent wake further from the channel centerline where $R_{0.1,0}$ is measured and thus coincides with the rapid decreases in the retardation following each maximum. For the highest Wi presented ($Wi \gg Wi_2$, red line) the time dependence of the flow is much less regular and only occasional random pulses are observed in the retardation signal over time.

The power spectra of the asymmetry parameter, $S_f(I)$, and the retardation, $S_f(R)$, are plotted against frequency in Figure 5g,h, respectively, where frequency has been scaled by the Maxwell relaxation time. For the highest and lowest Wi shown (black, blue, and red lines) the power spectrum shows random noise, with no clear dominant frequency content. However, for the intermediate case at $Wi \gtrsim Wi_2$ when the flow is asymmetric and highly periodic in time (green line), there is a strong peak in

both $S_f(I)$ and $S_f(R)$ at $f\lambda \approx 1$ and subsequent higher harmonics are clearly discernable up to $f\lambda \approx 10$. This is consistent with a previous study on this WLM system around rigid microposts[18] and strongly indicates that the temporal dynamics are governed by the Maxwell relaxation time of the WLM fluid.

2.3.4. Time-Dependent Oscillations of the Single Cylinder

By high speed video imaging of the free ends of the cylinders, we also analyze their time-dependent motion under various states of flow. Results from observations of the SC post at three representative Weissenberg numbers are presented in **Figure 6**. We define the displacement of the tip of the cylinder from its mean position in the x and y-directions (respectively) by $X^* = X - \overline{X}$ and $Y^* = Y - \overline{Y}$, where $\overline{X}$ and $\overline{Y}$ are the respective mean values. In Figure 6a–c, X^* and Y^* are plotted as a function of time at progressively increasing Wi, where the subtracted mean positions ($\overline{X}$ and $\overline{Y}$) are cited within the respective subfigures. Note that when the flow is started at a given Wi, there is an initial ≈ 30 s transient state in the motion of the post
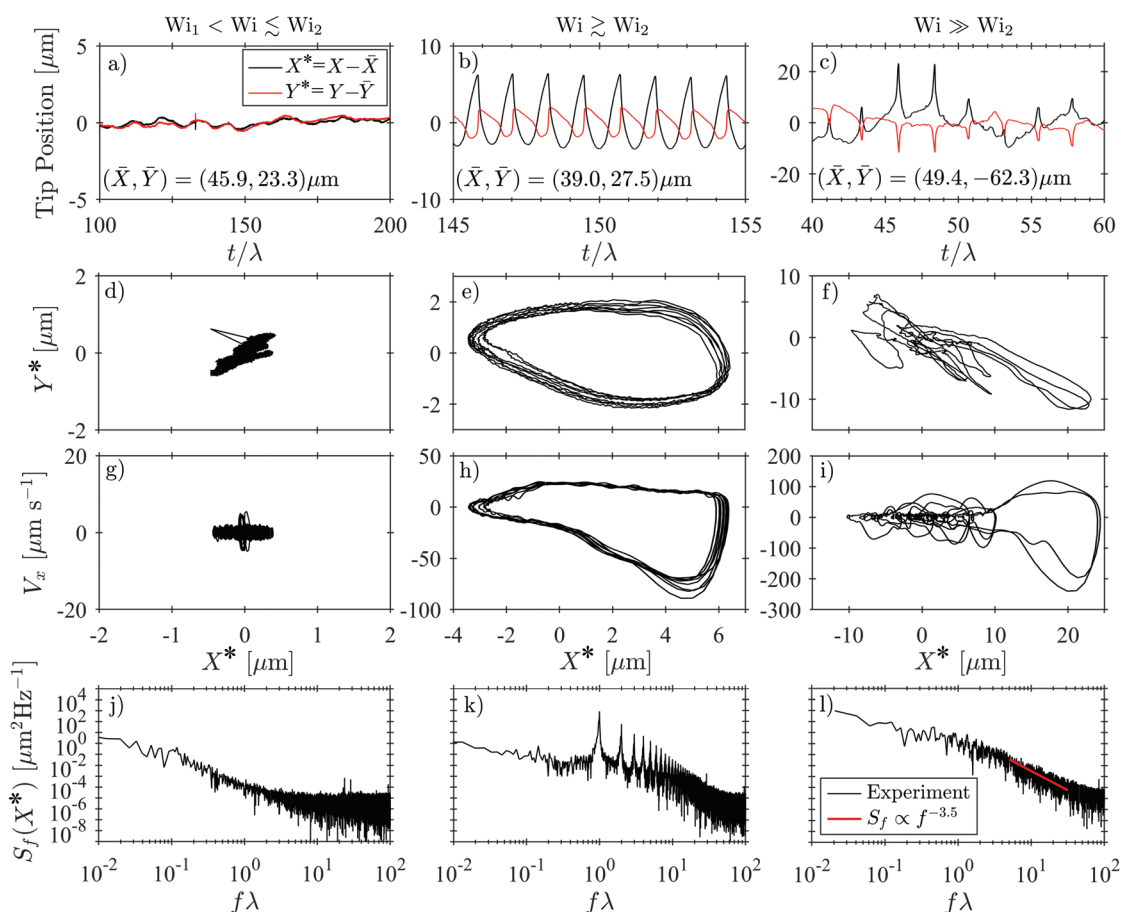
Figure 6. Analysis of time-dependent motions of the cylinder measured in the SC flow channel at three representative values of the Weissenberg number. a–c) Time series of the tip position in X^* and Y^*. d–f) Y^* versus X^* orbits over the same timespan shown in (a)–(c). g–i) Position–velocity phase plots for the motion in the x-direction. j–l) Power spectra derived from the X^* position time series.

that we do not show, rather we display a snapshot in time that illustrates the general behavior observed subsequent to the initial transient. Movies S7–S9 of the post behavior at each Wi are provided in the Supporting Information. In Figure 6d–f, the X^*-Y^* trajectory of the tip of the post at each imposed Wi is presented. In Figure 6g–i, position–velocity phase space plots of the x-component of the cylinder velocity, V_x as a function of X^* are plotted over the same span of time shown in Figure 6a–c. In Figure 6j–l, power spectra of the time series, $S_f(X^*)$, are plotted as a function of $f\lambda$ over the full post-transient duration of the experiment. In contrast to the power spectra in Figure 5, which were plotted on log-linear axes, here we plot on a log–log scale in order to highlight the strong power-law decay of $S_f(X^*)$ at high frequency discussed below.

For $Wi_1 < Wi \lesssim Wi_2$ (Figure 6a,d,g,j), the flow is asymmetric and steady, and the post deflects in both the x and y directions to a position that does not vary significantly in time (Figure 6a). The X^*-Y^* and position–velocity phase space plot shown in Figure 6d,g (respectively) are effectively single points. The power spectrum $S_f(X^*)$ at this Wi is plotted in Figure 6j and shows relatively low-amplitude spectral content that decreases in amplitude for increasing frequency to a plateau at high frequency.

For $Wi \gtrsim Wi_2$ (Figure 6b,e,h,k) when the flow is asymmetric and highly periodic in time (as shown in Figure 5), both X^* and

Y^* also oscillate periodically in time (Figure 6b). The X^* position traces out a sawtooth-like shape and the Y^* position traces out a reverse sawtooth-like shape. X^* increases gradually to a maximum, rapidly rebounds back in the $-x$ direction, then slowly changes direction and repeats the motion. The Y^* position follows an opposite pattern; a rapid increase in Y^* is followed by a gradual decrease before the pattern repeats. The rapid increase in Y^* away from the axis of the channel occurs simultaneously with the rapid decrease in X^*. This results in an almost elliptical motion of the post as shown by Figure 6e. Dey et al.[12] reported 1D oscillations prior to the flow becoming asymmetric with 2D elliptical motion. We note that we do not observe this 1D time-dependent regime, instead we observe the steady asymmetric deflection of the post prior to the development of time dependence and 2D oscillations. Although the 2D motion that we observe is far more regular than that reported by Dey et al,[12] we believe the underlying cause is similar. As elastic stress grows in the fluid, the post is dragged downstream and toward the center of the channel. The buildup of stress has a finite lifetime due to the relaxation of the wormlike micelles. Through a combination of the scission and reptation of individual micelles, on a time scale governed by the Maxwell relaxation time, the entangled micelles undergo a periodic process of fracturing, reformation, and stress build-up that drives the periodic motion of the cylinder.

ADVANCED
SCIENCE NEWS
www.advancedsciencenews.com

NANO · MICRO
small
www.small-journal.com

The position–velocity phase-space plot shown in Figure 6h reveals a regular orbit in the V_x versus x plane. The orbit travels in the clockwise direction. The large lobe at $-V_x$ corresponds to the rapid rebound of the X^* position of the cylinder. Although the phase-space orbit is very regular, the path it traverses does not exactly reproduce earlier paths.

The power spectrum plotted in Figure 6k reveals a strong fundamental peak at $f\lambda \approx 1$, i.e., at a frequency equal to the inverse of the Maxwell relaxation time. Similar to the power spectra plotted in Figure 5g,h at comparable Wi, higher harmonics up to $f\lambda \approx 20$ can be discerned in the spectrum. Additional characterization of amplitude and frequency of the oscillation of the post with respect to Wi is provided in the Supporting Information. The square of the amplitude of the oscillations, and the square of the fundamental frequency component, were found to decrease linearly with increasing Wi. This behavior is indicative of a subcritical Hopf bifurcation, in agreement with our previous study on the flow of the same WLM fluid past fixed microcylinders.[18] These results strongly suggest that the time-dependent dynamics of the post are driven by the interaction with the fluctuations in the flow field due to the flow instability. Since the flow is at negligible Re and relatively high Wi (here $Re \approx 10^{-6}$, $Wi \approx 173$, and $El \approx 10^8$), this could be referred to as a "purely-elastic" fluid–structure interaction.

The final case shown is for $Wi \gg Wi_2$ (Figure 6c,f,i,l), when the flow is asymmetric and time dependent but less regular than at lower Wi. The X^* and Y^* positions of the tip of the cylinder are plotted in Figure 6c. Their time dependence is erratic, with seemingly periodic spikes overlaid on a background motion that does not have a clear trend. Interestingly, in contrast to the previous case plotted in Figure 6b, where Y^* inversely follows X^*, here X^* and Y^* closely mirror each other; a spike in X^* to an increased downstream position is accompanied by a similar spike in Y^* further off-axis. Consequently, the X^*-Y^* plot in Figure 6f depicts an essentially diagonal to-and-fro motion of the cylinder. The time between the spikes in Figure 6c ($\approx$2.5 s) is longer than the period of the regular oscillations observed at lower Wi and, interestingly, is commensurate with the estimated reptation timescale of the micelles ($\approx$2.3 s).[23,24]

The position–velocity phase space plot in Figure 6i shows a complex lobe-like shape similar to that shown in Figure 6h. The orbit travels in the clockwise direction. The two large lobes at large X^* correspond to the two largest peaks in Figure 6c at $t \approx 46$ s and 48 s. For the two largest peaks, the rebound velocity is roughly two times larger in magnitude than the velocity during the initial pulse. This suggests that the buildup of stress on the post occurs more slowly than its relaxation, in agreement with the periodic motion at lower Wi. Although there is a similar repeating shape to the phase-space orbit, the regularity of the orbit seen at lower Wi is clearly not present anymore.

The power spectrum $S_f(X^*)$ for this high $Wi \gg Wi_2$ case is plotted in Figure 6l. Although there are seemingly periodic peaks in the X^* plot in Figure 6c, this does not manifest as a strong spectral peak anywhere in $S_f(X^*)$. There is a large-amplitude broad spectrum signal at low frequency, with the amplitude of $S_f(X^*)$ roughly a thousand times larger than in the lower Wi cases. The most striking observation in this power spectrum is the steep power-law decay of $S_f(X^*)$ at high

frequency. A red line with slope -3.5 is plotted on top of the experimental data in Figure 6l. A power spectrum slope of -3.5 has been observed in previous studies of the flow of polymer solutions and is characteristic of elastic turbulence.[6,25] Considering that $Re \ll 1$ and the motion of the post is a response to fluctuations within the flow due to elasticity, we suggest that our results may be evidence of elastic turbulence. Using numerical simulation, Rosti et al.[26] have described quantifying turbulent fluctuations by tracking the motion of flexible objects translating in the flow. Our results would constitute the first experimental use of a flexible structure for quantifying fluid fluctuations in elastic turbulence.

2.3.5. Coupled Time-Dependent Oscillations of the Double Cylinders

An analysis of the time-dependent motion of the DC system at three representative values of Wi is presented in **Figure 7**. The X^* positions of both cylinders are plotted in Figure 7a–c. Similarly, Y^* for both cylinders are plotted in Figure 7d–f. Similar to our analysis of the SC system, we plot the positions of the cylinders over a small range of time subsequent to the initial transient that occurs at startup. As before, Movies S10–S12 of the post behavior at each Wi are available in the Supporting Information. As can be seen in Figure 7a–f, the time-dependent motion of the cylinders appears to be highly synchronous, particularly for $Wi > Wi_2$. We quantify this similarity using the normalized cross-correlation function $C_{XY}(\tau)$, where $C = 1$ indicates perfect correlation, $C = -1$ indicates perfect anticorrelation, τ is the time lag between the two position-time series, and the pair of subscripts on C indicates which two position-time series are being cross-correlated. A time-resolved correlation function, $C_{XY}(t,\tau)$, is evaluated over a moving 10 s window to investigate how the correlation between the X (Figure 7g–i) and Y (Figure 7j–l) positions change in time. We also compute $C_{XY}(\tau)$ over the entire post-transient duration of the experiment to assess the overall correlation between the cylinders at a given Wi (Figure 7m–o).

The first case for $Wi_1 < Wi \lesssim Wi_2$, when the flow is asymmetric and steady in time, is illustrated by Figure 7a,d,g,j,m. The X^* and Y^* positions of the cylinders (Figure 7a,d, respectively) are steady within $\approx\pm$ 1 µm. There are small, seemingly random, variations in the X^* position of DC$_1$ that are not seen in the X^* position of DC$_2$. The Y^* position of DC$_1$ likewise displays an erratic variation in time, but here the motion is mirrored by DC$_2$. Note the subtracted mean values ($\overline{X}$ and $\overline{Y}$) are cited within the respective figures. The value of $\overline{X}_2$ (corresponding to DC$_2$) is significantly lower than that of $\overline{X}_1$ (corresponding to DC$_1$). On the other hand, $\overline{Y}_1$ and $\overline{Y}_2$ are approximately the same. This indicates that although DC$_1$ strongly shields DC$_2$ from streamwise drag, as shown in Figure 5, the perpendicular component of the force on DC$_2$ due to the asymmetric flow is not impeded by the upstream cylinder.

Figure 7g shows that for $\tau \approx 0$, there are random moments in time when the X position is strongly correlated ($C_{X_1X_2}(t,\tau) \approx 1$), but there is no clear trend in t or τ. $C_{Y_1Y_2}(t,\tau)$, plotted in Figure 7j, illustrates that the Y positions of the cylinders are strongly correlated at $\tau \approx 0$ over most of the time range plotted,
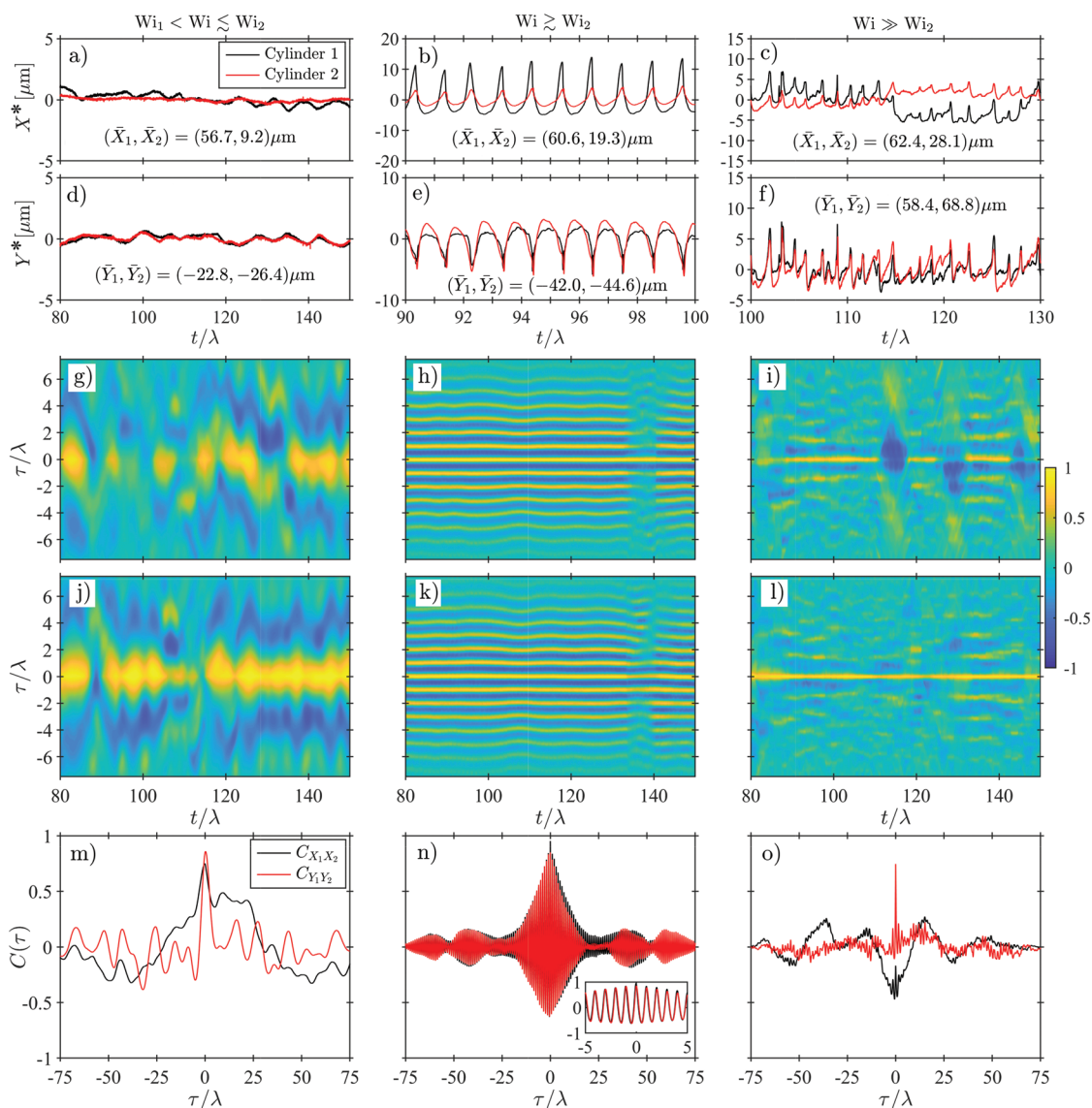
Figure 7. Analysis of time-dependent motions of the two cylinders measured in the DC flow channel at three representative values of the Weissenberg number. a–c) Time series of the X^* positions of the cylinders. d–f) Time series of the Y^* positions of the cylinders. g–i) Time-resolved correlation functions between the X positions of DC_1 and DC_2. j–l) Time-resolved correlation functions between the Y positions of DC_1 and DC_2. m–o) Full, post-transient, experimental time duration correlation functions between the X and Y positions of DC_1 and DC_2.

with only a few moments in time where the correlation falls appreciably below 1.

The cross-correlation functions calculated over the full duration of the experiment (Figure 7m), show that although both $C_{X_1X_2}(\tau)$ and $C_{Y_1Y_2}(\tau)$ are greatest for $\tau \approx 0$, the correlation between the Y positions (red curve) is stronger, while at larger time lags the correlation in both X and Y becomes weak.

The second case is for $Wi \gtrsim Wi_2$, i.e., when the flow is asymmetric and strongly periodic in time (Figure 7b,e,h,k,n). The X^* and Y^* positions of the cylinders, plotted in Figure 7b,e, respectively, show periodic oscillations in time similar to that seen for the SC system shown in Figure 6. Like the case at lower Wi, the $\bar{X}$ values for the two cylinders demonstrates that DC_1 continues to strongly shield DC_2 from streamwise drag, however

their $\bar{Y}$ values are approximately the same. The X^* positions of both cylinders trace out a sawtooth-like shape, with the amplitude of the oscillations of DC_1 being larger than that of DC_2. This is likely another consequence of the shielding of DC_2 by DC_1. Their Y^* positions, on the other hand, vary in time almost identically. As in the SC case, when the cylinders rebound in the $-x$ direction, they deflect rapidly in the $-y$ direction. In contrast with the SC case however, the two cylinders rapidly, rather than gradually, return to lower Y^*. The time-dependent correlation functions shown in Figure 7h,k demonstrate strongly periodic oscillations in correlation amplitude with increasing or decreasing τ that does not significantly change in time. As in the SC case, the period of the oscillations of the cylinders is approximately equal to the Maxwell relaxation time, so the

ADVANCED
SCIENCE NEWS
www.advancedsciencenews.com

NANO · MICRO
small
www.small-journal.com

variation in $C_{X_1X_2}$ and $C_{Y_1Y_2}$ with increasing or decreasing τ also has a period approximately equal to λ. The strong periodic variation in the cross-correlation functions persists over the full duration of the experiment, as shown in Figure 7n. The inset of Figure 7n shows a magnified view of the cross-correlation functions for $-5 < \tau\lambda < 5$, highlighting the strong periodic nature of $C_{X_1X_2}$ and $C_{Y_1Y_2}$ with a period approximately equal to λ. The amplitude of the oscillations of C decreases with increasing or decreasing τ, indicating that the further in time the signals are separated, the less similar their motions are.

The positions of the cylinders at $Wi \gg Wi_2$ are plotted in Figure 7c,f. Both the X^* and Y^* positions show erratic spiking behavior like that seen in the SC case at a similar Wi (Figure 6c). Note that a longer span of time is being plotted here compared to that shown in Figure 6c. As in the previous two cases, $\overline{X}_2 < \overline{X}_1$ due to streamwise shielding. However, $\overline{Y}_2 > \overline{Y}_1$, indicating that the y component of the elastic stress is stronger at DC_2. This may be due to the more rapid deflection of the highly stressed birefringent strand toward the side wall downstream of DC_2 that can be seen in Figure 4f. The time span shown in Figure 7c was explicitly chosen to highlight the separation of the X^* positions of the cylinders at around $t \approx 147$ s. This anticorrelation behavior manifests as a region of $C_{X_1X_2}(t,\tau) < 0$ shown in Figure 7i. Indeed, the time dependence of $C_{X_1X_2}(t,\tau)$ shows irregular spans of high correlation amplitude at $\tau \approx 0$ in addition to regions of time with low or negative correlation amplitude. For increasing or decreasing τ there are small spans of time when periodic oscillations in $C_{X_1X_2}(t,\tau)$ can be seen, however for the most part there is no clear pattern. $C_{Y_1Y_2}(t,\tau)$, on the other hand, plotted in Figure 7l, shows high correlation amplitude at $\tau \approx 0$ for the entire duration of the experiment. Like for $C_{X_1X_2}(t,\tau)$, there are short moments of periodicity for increasing or decreasing τ, but for the most part no clear pattern can be seen. Perhaps the most striking observation at this Wi is in the cross-correlation functions evaluated over the full duration of the experiment, shown in Figure 7o. The cross correlation of the Y positions reveals strong positive correlation at $\tau \approx 0$, with random low-amplitude oscillations for increasing or decreasing τ. The cross correlation of the X positions shows weak anticorrelation for $\tau \approx 0$ with low-amplitude long-period oscillation for increasing or decreasing τ. Similar to the regular spikes in the position time series for the SC at high Wi (Figure 6c) that did not manifest as a strong peak in the power spectrum (Figure 6f), the seemingly regular spikes in the X and Y positions of the two cylinders (Figure 7c,f) do not yield periodic high amplitude contributions to the cross correlation function that are seen at lower Wi (Figure 7h,k,n). This indicates that although the Maxwell relaxation time is responsible for the periodic motion of the cylinders for $Wi \gtrsim Wi_2$, for high enough Wi it is no longer the dominant timescale and some slower dynamical process, such as reptation is driving the instability in the flow and the consequent motion of the cylinders.

Considering the highly correlated intermediate $Wi \gtrsim Wi_2$ case, we note that the maximum correlation amplitude does not occur at precisely $\tau = 0$. For streamwise displacements (i.e., X) the maximum value of $C_{X_1X_2}$ occurs at $\tau \approx -50$ ms, indicating that DC_2 lags DC_1 by 50 ms. The separation distance between the cylinders during the experiment δx, gives an approximate wave speed $V_{wave} = \delta x / \tau \approx 7.2$ mm s^{-1}. For this experiment, the

average flow speed was $V_{avg} = 4.2$ mm s^{-1} and the speed of the fluid passing above (or below) the cylinders is up to $\approx 2.5 \times V_{avg}$. The time lag between the X positions of the cylinders can thus be rationally attributed to streamwise advection of the fluid. However, for $C_{Y_1Y_2}$, the correlation peak occurs between 0 and -5 ms, at a time lag that is shorter than the time resolution of our experiments (which is limited by the video acquisition rate). This short time lag yields $V_{wave} \gtrsim 72$ mm s^{-1}, significantly larger than the speed of the fluid. We can estimate the elastic wave speed for this fluid via the viscoelastic Mach number $Ma = V_{avg}/V_{El} = \sqrt{WiRe}$, which gives $V_{El} \approx 160$ mm s^{-1}. This would yield an expected time lag of $\tau \approx -2.2$ ms, commensurate with our estimate. This strongly indicates that the changes in the Y positions of the cylinders are dominated by the elastic stress in the fluid rather than by fluid advection between the cylinders. Indeed, the cylinders would not deflect in the y direction at all without the presence of elastic stress. We propose that the system can be thought of as two cylinders connected by a stressed elastic filament. Together with fluid advection, the complex coupled motion of the cylinders is driven by changes in the tensile stress that propagate along the filament as an elastic wave.

3. Conclusion

In this work, we have studied the fluid–structure interaction between cantilevered microcylinders and a shear-banding viscoelastic fluid consisting of wormlike micelles. Owing to the small size of the microcylinders, the Reynolds number is negligible, but the Weissenberg number is comparatively large, providing a flow elasticity number $El \approx 10^8$. This is characteristic of the elasticity expected in mucociliary flow and indicates that elastic forces dominate the system response.

Of the variety of flow phenomena we report, perhaps the most interesting occur in the intermediate regime of Weissenberg number where the flow becomes time-dependent in a very regular way with a fundamental frequency equal to the inverse of the fluid relaxation time. Under these conditions, a single cantilevered micropost beats at the same characteristic frequency as the fluid, and a pair of cantilevered microposts beat in near-perfect synchrony in both the streamwise and transverse directions. Oscillations transverse to the flow direction are most correlated at a time lag much shorter than can be explained by the advection of fluid along the channel. Instead, we propose that the cylinders are physically connected by a highly stressed elastic filament. Our results suggest that the complex motion of the coupled cylinders is driven by changes in the tensile stress along the filament that propagate as an elastic wave. Interesting avenues for future research that would allow this phenomenon to be understood more deeply, could be to vary the flexibility of the microcylinders by tuning their lengths and/or radii, and to investigate how the flow instability and resulting collective motion of two, or more, microcylinders depends on their separation distance.

This study was largely motivated by the motion of slender bodies in biological systems (e.g., cilia in mucus). In our model experimental system, the cantilevered posts are passive

and their periodic motion arises due to a fluid instability likely related to the breakage and reformation of micellar structures. Fluid instabilities are also likely to occur in real viscoelastic biological fluid flows and feedback on the motion of deformable translating microstructures like cilia and flagella. However, in biology the structures of interest are usually actively driven in a cyclic fashion, thus injecting periodic motion to the fluid. Whether the fluid is driven past the structure, or the structure is driven through the fluid, our study shows that the presence of localized elastic stresses in the fluid can effectively link the immersed structures together, contributing to their collective dynamics. Previous studies have mostly focused on the low Reynolds number hydrodynamical interactions between the cilia and the surrounding biological fluids. However, the purely-elastic effects that we report will be important to consider in achieving a more complete understanding of the complex motions seen in biological systems.

4. Experimental Section

Test Fluid Preparation: The Newtonian test fluid employed in control experiments was a 95 wt% solution of glycerol in deionized (DI) water, viscosity $\eta = 0.374$ Pa s, $\rho = 1245.7$ kg m^{-3} at 24 °C.

The viscoelastic test fluid was composed of 100×10^{-3} M of the cationic surfactant cetylpyridinium chloride (CPyCl, Sigma-Aldrich) and 60×10^{-3} M of the organic salt sodium salicylate (NaSal, Sigma-Aldrich) dissolved in DI water. This surfactant and counterion system is well known to form a viscoelastic solution of entangled WLMs, with a single characteristic relaxation time.[27,28] The solution was prepared by adding the appropriate mass of DI water to the combined weighed quantities of CPyCl and NaSal dry powders and stirring vigorously for 7 d. Subsequently, the fluid was stored in dry unlit conditions at 24 °C (above the Krafft temperature below which precipitation occurs) for 10 d to ensure the formation of equilibrium WLM structures prior to experimentation. Full details of the fluid properties and rheology are provided in the Supporting Information.

Microdevice Fabrication and Flow Control: Microchannels containing flexible cylinders attached to one wall were etched inside a single piece of 5 mm thick fused silica glass by the high resolution ($\approx O(1 \ \mu m)$) technique of SLE.[16–18,29]

Following SLE fabrication, tubing connectors were bonded to the inlet and outlet holes using a 2-part epoxy resin. Poly(ethyl ether ketone) (PEEK) tubing was used to connect the inlet and the outlet of the device to gastight syringes (Hamilton, NV). Flow through the device was driven at controlled volumetric flow rates using neMESYS syringe pumps (low pressure 29:1 gear ratio, Cetoni GmbH, Germany), ensuring a smooth and steady flow through the microchannel.

MicroParticle Image Velocimetry: Quantitative measurements of velocity vector fields were acquired using a volumetric microparticle image velocimetry (μ-PIV) system (TSI Inc., MN).[30,31] For this measurement, the test fluid was seeded with ≈0.02 wt% of fluorescent microspheres (1 μm diameter Fluoromax red, Thermo Scientific Inc.) that accurately followed the streamlines. The midplane of the flow geometry ($z = 1$ mm) was brought into focus on an inverted microscope (Nikon Eclipse Ti) using a 5 × Nikon PlanFluor objective lens (numerical aperture NA = 0.15). Under these conditions, the measurement depth over which microparticles contributed to the determination of the velocity field was $\delta z_m \approx 110$ μm (or $\approx 0.05H$),[30] and 2D velocity vectors on a square grid with spacing 25.6 × 25.6 μm were obtained. Processing of vector fields to compute streamlines, extract velocity profiles, etc., was performed offline using custom Matlab scripts. Further technical details of the methods are available in ref. [18].

Flow-Induced Birefringence Measurement: FIB was measured using a high speed polarization camera (CRYSTA PI-1P, Photron Ltd, Japan) installed on a home-built upright microscope. The camera features a "micropolarizer array" in front of a standard CMOS imaging sensor. The micropolarizer array consisted of 1024 × 1024 linear polarizing elements (each the size of one pixel of the 1024 × 1024 CMOS sensor) arranged in sets of 2 × 2 with orientations of 0°, 45°, 90°, and 135°. The microfluidic device was placed on the imaging stage of the microscope and the $z = 1$ mm plane was brought into focus using a 10 × Nikon PlanFluor objective lens. White light was passed through a 532 nm bandpass filter and a circular polarizer, before passing through the sample and being focused onto the imaging sensor of the camera through the micropolarizer array. By analyzing the light intensity received at the individual pixels in each 2 × 2 grouping, a spatially resolved (≈3 μm per pixel) and quantitative measurement of the retardation, R and orientation angle θ was obtained.[18,32,33]

High-Speed Video Microscopy and Cylinder Tracking: High speed video imaging (200 frames s^{-1}) of the motion of the cylinders was accomplished by focusing in the plane of the free end of the cylinders using an inverted microscope (Leica DMI 3000) and a Phantom Miro camera (Vision Research Inc.). High visual contrast between the cylinder and the fluid was achieved by adding a small amount (≈0.1 g mL^{-1}) of Rhodamine B to the fluid and observing the flow under blue-filtered light. The fluid thus appeared black and the post bright white (see Figure 2a). The tip of the cylinder was easily isolated in each frame by applying a pixel intensity threshold mask using MATLAB. The center position of the tip of the cylinder was then determined by calculating the center-of-mass of the high-value pixels, and was tracked in time.

COMSOL Multiphysics Flow Simulation: The flow of a Carreau–Yasuda fluid past a 2D cylinder using COMSOL Multiphysics, a commercial finite element numerical simulation software package was simulated.[34] Steady-state simulations were done using the Laminar Flow module. The "User Defined" dynamic viscosity setting was used to program the Carreau–Yasuda model into the simulation according to the experimentally measured fluid properties. In the simulation, the width of the channel was 400 μm and its length was 4000 μm. The cylinder, modeled as a circle, was situated at the center of the channel. The no-slip boundary condition was imposed on the surfaces of the channel and cylinder. Equal and opposite pressures were applied at the inlet and outlet to generate the flow. The flow rate at each pressure was determined by calculating the average flow velocity near the inlet and using $Q = HWV_{avg}$. The predicted stress on the cylinder was calculated by integrating the stress per unit length, readily provided by COMSOL, around the circumference of the circle and then multiplying by the length of the physical cylinders used in the experiment.

Supporting Information

Supporting Information is available from the Wiley Online Library or from the author.

Conflict of Interest

The authors declare no conflict of interest.

[1] D. J. Beebe, G. A. Mensing, G. M. Walker, *Annu. Rev. Biomed. Eng.* **2002**, *4*, 261.

[2] G. M. Whitesides, *Nature* **2006**, *442*, 368.

[3] E. K. Sackmann, A. L. Fulton, D. J. Beebe, *Nature* **2014**, *507*, 181.

[4] E. M. Purcell, *Am. J. Phys.* **1977**, *45*, 3.

[5] S. Camalet, F. Jülicher, J. Prost, *Phys. Rev. Lett.* **1999**, *82*, 1590.

[6] A. Groisman, V. Steinberg, *Nature* **2001**, *410*, 905.

[7] A. Groisman, M. Enzelberger, S. R. Quake, *Science* **2003**, *300*, 955.

[8] A. Groisman, S. R. Quake, *Phys. Rev. Lett.* **2004**, *92*, 094501.

[9] S. K. Lai, Y.-Y. Wang, D. Wirtz, J. Hanes, *Adv. Drug Delivery Rev.* **2009**, *61*, 86.

[10] D. J. Smith, E. Gaffney, J. Blake, *Bull. Math. Biol.* **2007**, *69*, 289.

[11] A. A. Dey, Y. Modarres-Sadeghi, J. P. Rothstein, *J. Fluid Mech.* **2017**, *813*, R5.

[12] A. A. Dey, Y. Modarres-Sadeghi, J. P. Rothstein, *Phys. Rev. Fluids* **2018**, *3*, 033303.

[13] R. Golestanian, J. M. Yeomans, N. Uchida, *Soft Matter* **2011**, *7*, 3074.

[14] J. Elgeti, G. Gompper, *Proc. Natl. Acad. Sci. USA* **2013**, *110*, 4470.

[15] M. H. Sedaghat, M. M. Shahmardan, M. Norouzi, M. Nazari, P. G. Jayathilake, *Math. Biosci.* **2016**, *272*, 44.

[16] J. Gottmann, M. Hermans, J. Ortmann, *Phys. Procedia* **2012**, *39*, 534.

[17] N. Burshtein, S. T. Chan, K. Toda-Peters, A. Q. Shen, S. J. Haward, *Curr. Opin. Colloid Interface Sci.* **2019**, *43*, 1.

[18] S. J. Haward, N. Kitajima, K. Toda-Peters, T. Takahashi, A. Q. Shen, *Soft Matter* **2019**, *15*, 1927.

[19] H. A. Stone, C. Duprat, in *Fluid-Structure Interactions in Low-Reynolds-Number Flows* (Eds: C. Duprat, H. A. Stone), The Royal Society of Chemistry, Cambridge **2016**, Ch. 2.

[20] J. M. Gere, S. P. Timoshenko, *Mechanics of Materials*, 3rd ed., Chapman & Hall, London **1991**.

[21] H. J. McSkimin, *J. Appl. Phys.* **1953**, *24*, 988.

[22] J. N. Israelachvili, *Intermolecular and Surface Forces: With Applications to Colloidal and Biological Systems*, Academic Press, London **1985**.

[23] M. E. Cates, *Macromolecules* **1987**, *20*, 2289.

[24] M. S. Turner, M. E. Cates, *Langmuir* **1991**, *7*, 1590.

[25] A. Varshney, V. Steinberg, *Nat. Commun.* **2019**, *10*, 652.

[26] M. E. Rosti, A. A. Banaei, L. Brandt, A. Mazzino, *Phys. Rev. Lett.* **2018**, *121*, 044501.

[27] H. Rehage, H. Hoffmann, *J. Phys. Chem.* **1988**, *92*, 4712.

[28] H. Rehage, H. Hoffmann, *Mol. Phys.* **1991**, *74*, 933.

[29] G. Meineke, M. Hermans, J. Klos, A. Lenenbach, R. Noll, *Lab Chip* **2016**, *16*, 820.

[30] C. D. Meinhart, S. T. Wereley, M. H. B. Gray, *Meas. Sci. Technol.* **2000**, *11*, 809.

[31] S. T. Wereley, C. D. Meinhart, *Annu. Rev. Fluid Mech.* **2010**, *42*, 557.

[32] G. G. Fuller, *Optical Rheometry of Complex Fluids*, Oxford University Press, New York **1995**.

[33] J. A. Odell, in *Handbook of Experimental Fluid Mechanics*, (Eds: C. Tropea, A. L. Yarin, J. F. Foss), Springer-Verlag, Heidelberg **2007**, pp. 724–732.

[34] COMSOL, Inc., http://www.comsol.com (accessed: June 2018).